PAPER

Check for updates

Synthesis of centimeter-scale high-quality polycrystalline hexagonal boron nitride films from Fe fluxes†

Yifei Li, [a] Xin Wen, [a] Changjie Tan, [a] Ning Li, [b,c] Ruijie Li, [a] Xinyu Huang, [a] Huifeng Tian, [a] Zhixin Yao, [a,d] PeiChi Liao, [a] Shulei Yu, [a] Shizhuo Liu, [a] Zhenjiang Li, [a] Junjie Guo, [d] Yuan Huang, [e] Peng Gao, [b,c,f] Lifen Wang, [g,h] Shulin Bai [a] and Lei Liu *[a,f]

High-quality hexagonal BN (hBN) crystals, owing to their irreplaceable roles in new functional devices such as universal substrates and excellent layered insulators are exceedingly required in the field of two-dimensional (2D) materials. Although large-scale monolayer hBN crystals have been successfully grown on catalytic metals, the synthesis of large-area continuous hBN films with thickness in microns is challenging, hindering their applications at the mesoscopic level. Herein, we report the single-metal flux growth of centimeter-large, micron-thick, and high-quality continuous hBN films by balancing the grain size and coverage. The as-grown films can be readily exfoliated and transferred onto arbitrary substrates. Isotopically engineered hBN crystals can be obtained as well by the method. The narrow Raman line widths of the intralayer E_{2g} mode peak (2.9 cm^{-1} for h^{11}BN, 3.3 cm^{-1} for h^{10}BN, and 7.9 cm^{-1} for h^{Na}BN) and ultrahigh thermal conductivity (830 W m^{-1} K^{-1} for 4L h^{11}BN) demonstrate high crystal quality and low defect density. Our results provide the foundation for the cost-efficient and lab-achievable synthesis of high-quality hBN films aimed at its mesoscopic applications.

1. Introduction

Hexagonal boron nitride (hBN) possesses a wide bandgap (larger than 5.5 eV) and an atomically flat, almost defect-free surface without dangling bonds, making hBN the unmatched candidate as an ideal substrate for other two-dimensional (2D) crystals.[1–5] For instance, graphene monolayers exhibit ultra-high room-temperature mobility comparable to the phonon-scattering theoretical limit when sandwiched by hBN layers.[2,3] Moreover, hBN serves as one irreplaceable building block in van der Waals (vdW) heterostructures by protecting air-sensitive 2D materials and working as an electrically insulating layer along the *z*-direction.[4,5] While 2D layers of hBN have been intensely investigated over the last decade, much less noticeable but equivalently significant is its "more bulk" polymorph, such as micron-thick hBN films and relevant mesoscopic applications.

As one of the conventional ceramics, the hBN film holds several remarkable physical and chemical properties to underpin its versatile applications ranging from thermal conduction to thermal neutron detection. Due to its excellent dielectric and thermal properties (in-plane thermal conductivity: ∼550 W m^{-1} K^{-1}), hBN is a promising candidate for heating dissipation devices, especially in scenarios requiring electrical insulation.[6–11] While hBN sheet-based composites suffer from interface thermal resistance, a continuous three-dimensional (3D) hBN skeleton grown by chemical vapor deposition (CVD) provides uninterrupted thermal channels for superior thermal conduction.[12,13] Moreover, hBN has been demonstrated as a strong candidate of far-ultraviolet (FUV, wavelengths: 280–198 nm) fluorescent materials.[14] Furthermore, ^{10}B, as one

[a]School of Materials Science and Engineering, Peking University, Beijing 100871, China. E-mail: l_liu@pku.edu.cn

[b]International Center for Quantum Materials, School of Physics, Peking University, Beijing 100871, China

[c]Electron Microscopy Laboratory, School of Physics, Peking University, Beijing 100871, China

[d]Key Laboratory of Interface Science and Engineering in Advanced Materials, Ministry of Education, Taiyuan University of Technology, Taiyuan 030024, P. R. China

[e]Advanced Research Institute of Multidisciplinary Science, Beijing Institute of Technology, Beijing, 100081, China

[f]Interdisciplinary Institute of Light-Element Quantum Materials and Research Center for Light-Element Advanced Materials, Peking University, Beijing 100871, China

[g]Beijing National Laboratory for Condensed Matter Physics, Institute of Physics, Chinese Academy of Sciences, Beijing 100190, China

[h]Songshan Lake Laboratory for Materials Science, Dongguan 523000, China

†Electronic supplementary information (ESI) available. See DOI: 10.1039/d1nr02408f

of the three elements holding significant neutron scattering efficiency (other two: ^{3}He and ^{6}Li), exhibits its own advantages, such as high stability and solid state.[15,16] Therefore, isotopically enhanced B compounds (h^{10}BN, especially) work as high-performance solid-state thermal neutron detectors.[15,16] For the aforementioned hBN applications beyond monolayers, large-scale and high-quality hBN films with thickness in microns and capability of isotope substitution can largely boost the device performance by, for instance, providing a large-sized plane-emission FUV source. Another example is that the absorption length of thermal neutrons can reach ~47 μm in h^{10}BN, requiring the comparable thickness of hBN films for high detector efficiency.[15]

Recent works have demonstrated the big success in the CVD growth of centimeter-scale monolayer hBN.[17,18] However, the ultra-high melting point of hBN (>2950 °C) and low vapor pressure of boron make the melt or vapor-phase synthesis of hBN films quite tricky and costly. To date, the metal flux growth at atmospheric pressure using binary metals as solvents such as Ni–Mo, Ni–Cr, Fe–Cr, and Cu–Cr, produced an excellent crystal whose quality is comparable with that of samples synthesized under high pressures and at high temperatures.[19–24] One of these two-component fluxes has high boron solubility, and the other is added to increase nitrogen solubility. Yano *et al.* discovered Na as a single-component flux for the growth of h-BN crystals at a low temperature, but requiring a high pressure.[25] Very recently, Li *et al.* have reported the successful synthesis of high-quality hBN crystals at atmospheric pressure using pure iron as a flux.[26] However, the challenge still remains to produce continuous large-sized hBN films using the flux method. Here, we introduce one low-cost flux growth of hBN assisted by Fe powders, producing the continuous square-centimeter film and isotopically enriched samples.

2. Results

The synthesis strategy of hBN crystals by using the Fe flux is shown in Fig. 1a. Ultrahigh-purity B (Alfa Aesar, 99.99%) and Fe (Alfa Aesar, 99.9%) powders are mechanically mixed and put into alumina boats that are highly stable and non-reactive at high temperatures. Alternative B sources used in the experiment are commercial hBN (Alfa Aesar, 99.99%) powders. Here, we note that compared with Cr and Mo powders, Fe powders with the same purity and grain sizes can easily cut the metal flux cost by at least 70%, showing its potential for massive preparation.

A laboratory single-zone tube furnace with the highest working temperature of 1700 °C and the 11 in. – long heating zone was used. For one synthesis route, a mixture of 100 g Fe and varied hBN powder was used as the source materials; in another route, 100 g of Fe is mixed with B powder. Source materials are loaded into the pre-baked alumina boat, followed by the transfer into a 2.4 in. – diameter alumina tube as the inner one to protect the one equipped in the furnace. Prior to

the growth, the whole chamber was evacuated down to 10 mTorr, and then filled with the nitrogen/hydrogen mixture (5% H$_2$ in N$_2$, UHP) and carrier gas (argon, UHP) back to atmospheric pressure. Nitrogen gas was utilized for nitride B powders, and hydrogen keeps reducing the atmospheric pressure during the reaction process. Since oxygen and carbon have been demonstrated as major impurities during the hBN crystal growth, which degrade the crystal quality by introducing extra defect levels, we repeated this "pump-refill" process three times to minimize the residual carbon and oxygen impurities in the system before growth. Instead of the oil vacuum pump, the turbo-pump station was highly recommended to eliminate hydrocarbon contaminations.[27] The heating cycle started with a quick ramping from room temperature to 1550 °C. Then, the sample stays at 1550 °C for 24–48 hours, ensuring precursors and Fe flux forming a complete solution. After that, slow cooling to 1450 °C at a rate of 4 °C per hour was applied to obtain high-quality crystals. The furnace was then quickly quenched (300 °C per hour) to room temperature. The temperature profile is shown in Fig. S1.† During all of these processes, the nitrogen/hydrogen mixture and carrier gases continuously flow at a rate of 95 and 5 sccm, respectively.

After the growth, Fe ingots obtained by melting and re-solidification processes were observed with precipitated hBN films on the surface, following the characterization of the metal flux growth (see Fig. S2† for a typical optical image before transfer). The zoomed-in image displayed in Fig. 1b shows the grain boundaries that roughly follow three directions with ~120 degree angles to each other, probably stemming from the energetically favored zigzag edges with nitrogen terminations at the microscopic level.[28–30] Compared with the bi-metal flux method, another benefit from the Fe solvent is the easy exfoliation of hBN films from metal ingots simply by immersing them into hydrochloride acid in about one hour (Fig. S3†). The floating hBN films were then thoroughly washed and dried. With the conventional tape exfoliation, hBN flakes with different thicknesses and lateral sizes of tens of microns can be obtained (Fig. 1c).[31]

We further compare the as-synthesized hBN films with commercial hBN products by Raman measurements. The Raman linewidth is associated with the phonon lifetime by the energy-time uncertainty relation $\tau^{-1} = \Gamma/\hbar$, where τ is the phonon lifetime, Γ is the full width at half maximum (FWHM, in cm^{-1}) of the Raman peak, and $\hbar$ is Planck's constant.[32] The crystal defects can reduce the phonon lifetime by scatterings; therefore, experimentally the Raman linewidth was frequently investigated to estimate the crystal quality. As shown in Fig. 1d, one symmetric Raman peak assigned to the in-plane E_{2g}^{high} mode was located at 1366 cm^{-1} with 7.9 cm^{-1} of FWHM for the as-synthesized hBN crystals. In addition, three commercial hBN samples show larger linewidths (8.6–9.7 cm^{-1}). We also notice the comparable Raman peak widths of the hBN crystal from the bi-metal flux growth (7.8 cm^{-1} for Ni–Cr flux samples), indicating the similar defects control in Fe-flux hBN crystals.[20] We thus conclude
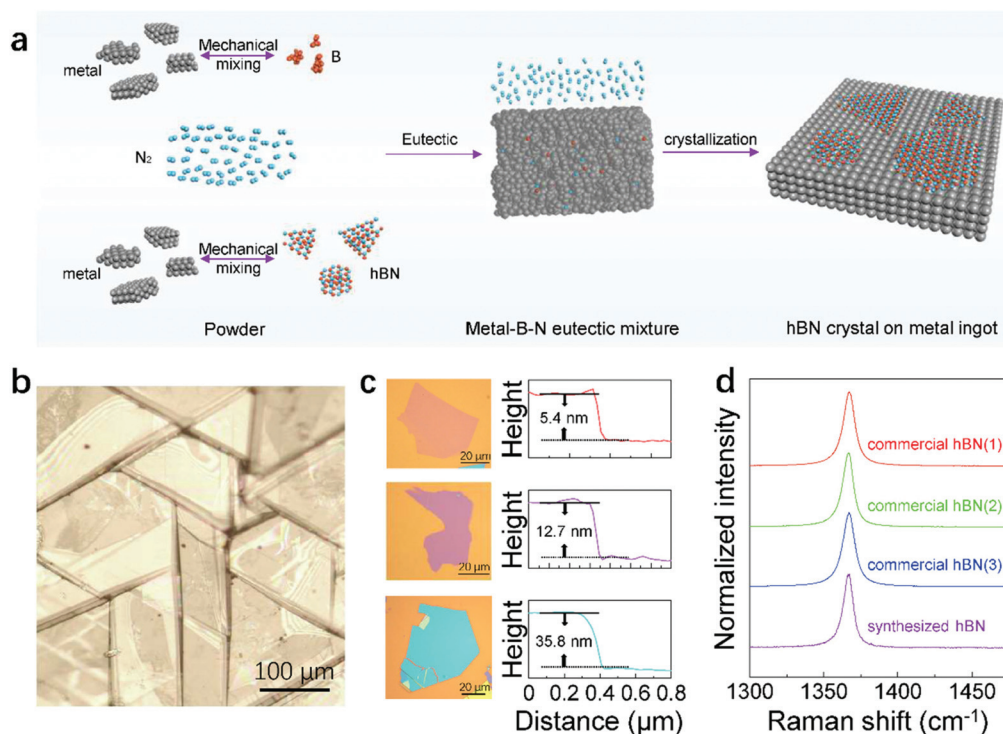
Fig. 1 hBN crystal growth from metal fluxes. a, Schematic of the procedure of hBN growth. b, Zoom-in optical image of hBN films showing grain boundaries that roughly follow three directions. c, Optical images (left panel) and the corresponding height profiles (right panel) from AFM characterizations of hBN flakes, showing varied thickness. d, Raman spectra of the in-plane E_{2g}^{high} mode from the as-synthesized hBN crystals and commercial ones.

that as-synthesized films and exfoliated hBN flakes have sufficient crystal quality for lab research use in the 2D materials field. For example, we have recently grown monolayer WS_2 on hBN flakes (Fe-flux samples), showing the high quality of the interface in this vdW heterostructure.

Moreover, practical applications demand large-scale, and more importantly, continuous hBN films to avoid device failures, for example, hole-induced defective pixels in the FUV plane source and top-to-bottom electrode leakage when used as a neutron detecting component. However, owing to the intrinsic anisotropy of the edge formation energy and near-equilibrium precipitation process in the metal flux growth, the typical morphology of hBN grains is an equilateral triangle, clearly proofed by the optical image of low-coverage samples (Fig. 2a). Consequently, gaps between hBN crystallites seem inevitable as the growth continues. Fig. 2b shows one as-grown hBN film with the apparent crack (200 μm in width), breaking the film continuity.

To overcome the crack during the growth, the effect of precursor/flux ratio, i.e., B atomic percent (%B), was systematically examined in our experiments. While the B–N–Fe ternary phase diagram is unknown, in the Fe–B phase diagram, the lowest eutectic temperature arises when the %B is equal to 16.2 at%.[33] Growths with gradually increased %B were thus performed; the estimated average grain sizes based on optical images and film continuity are summarized as a function of %

B in Fig. 2c. The growths with hBN powders as source materials were first examined, where %B remained below 6 at% (Fig. 2c top panel). When %B is less than 2.4 at%, the abnormal-growth-like behaviors were observed with apparent different regions on one ingot, showing larger crystallites (~30 μm) and small domains (~13 μm), respectively. The discrepancy of grain sizes on the same Fe ingot can be attributed to insufficient precursor supply, resulting in dynamically favored mass transport and growth at specific sites. This point is supported by observing the colorful surface of hBN films with uneven thickness when %B is less than 2.4 at% (Fig. S4†). By increasing %B (up to 5.3 at%), albeit the averaged crystallites' size keeps small, uninterrupted films with 100% coverage can be routinely obtained. Thus, exfoliated hBN films by the wet chemistry can be cut to regular shapes; as displayed in Fig. 2d and e, one rectangle hBN film in lateral dimensions of 2.5 cm by 1.5 cm was successfully loaded onto a piece of polydimethylsiloxane (PDMS), waiting for strain experiments by bending the substrates.

Another synthesis route uses B powders as precursors, where %B remained over 6 at% (Fig. 2c bottom panel). Experiments with different %B ranges were applied. While 7.8 at% of %B leads to similar hBN films with BN powder-growth, i.e., continuous films with ~10 μm of domain sizes, some grains increased up to 400 μm large and other crystallites keep smaller than 100 μm when %B approaches an eutectic point of
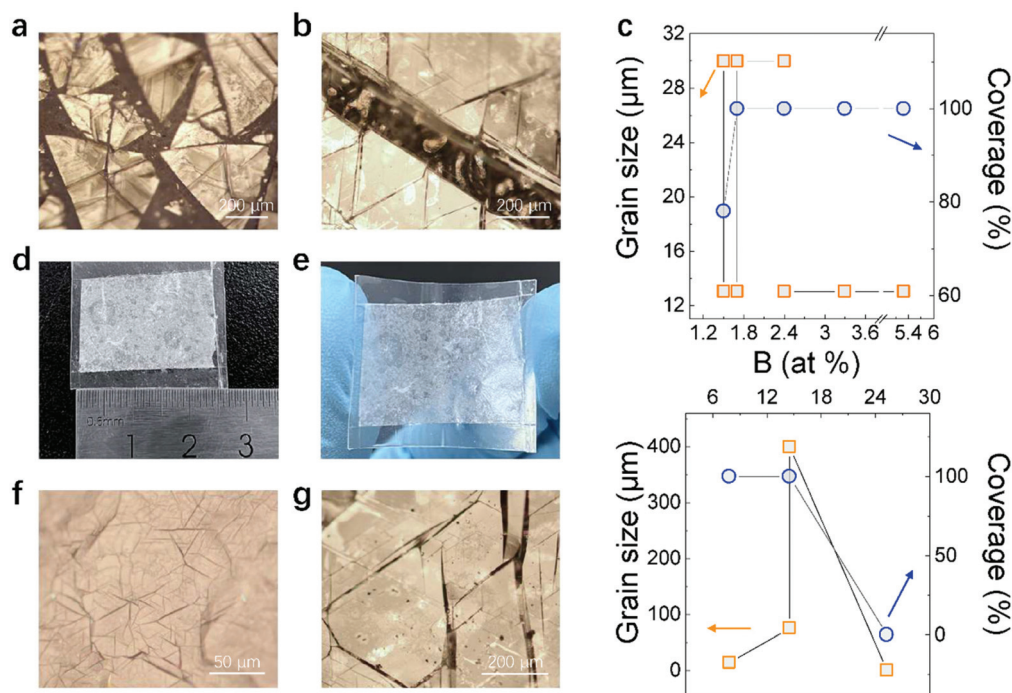
Fig. 2 Centimeter-scale high-quality hBN films based on the Fe flux growth. a and b, Optical images of the low-coverage hBN crystals (a) and the as-grown hBN films with an apparent crack (b). c, Statistics of the estimated average grain sizes and film coverage as a function of B atomic percent. The growth with hBN powders (top panel) and B powders (bottom panel) is displayed separately. d and e, Optical images of the exfoliated hBN film cut to the rectangle shape on one PDMS piece. f and g, Zoom-in micro-image of the as-grown hBN films with ~10 μm grain sizes (f) and ~400 μm grain sizes (g).

16.2 at% (Fig. 2f and g). Furthermore, increasing %B beyond 16.2 at% can introduce the total failure of hBN growth with the absence of B–Fe eutectics, showing original powder morphologies after the growth (Fig. S5†). The growth mechanism can be more complex when compared with one with hBN powders as precursors. The reaction dynamics include grabbing nitrogen atoms from the gas phase, dissolving, and forming covalent bonds with boron atoms in solutions. With lower boron loading (7.8 at% of %B), N atoms and nitrides are sufficient, creating a continuous film with a uniform grain size. However, when %B increases up to 14.5 at% (very close to 16.2 at%), we speculate that the nitriding reaction competition between different locations is more prominent since more B atoms are waiting for the nitrogenization, leading to uneven grain sizes. The total failure of the hBN growth meets the expectation. According to the phase diagram of B–Fe, a new phase, Fe_2B, can be involved when %B is more than 16.2 at%, inducing much more complex behaviors during homogenization and precipitation processes.[33]

To check the generality of the Fe-flux growth, isotopically engineered hBN crystals were synthesized using an ultrahigh isotopic purity of ^{10}B (97.18 at%) and ^{11}B (99.69 at%) powders as precursors without any other variations in growth parameters. By differing the atom mass, isotope engineering has been shown as a powerful means to tune lattice vibrations and electronic structures through electron–phonon couplings.[34] The recent experiments reveal more complex physics in isoto-

pically pure hBN crystals, including ultralow-loss polaritons and isotope-dependent vdW interactions.[35,36] The further explorations of isotopic effects at a larger scale, for example, ^{10}B-neutron interactions and consequent induced carrier transport, also obligate the high-quality and large-area hBN film with isotope tunability.

In addition, our results show the successful synthesis of isotopically engineered hBN crystals. Fig. 3a and b show the scanning transmission electron microscopic (STEM) images of h^{10}BN and h^{11}BN flakes, respectively, from the as-grown crystals. Perfect honeycomb lattices without apparent defects or lattice distortions were observed, suggesting high crystal qualities. Lattice constants were measured based on intensity profiles, and no discrepancy was observed between h^{10}BN and h^{11}BN samples, meeting our expectations. The consequence of isotope engineering on lattice vibrations can be confirmed by probing the phonon spectrum. Benefiting from the ultrahigh energy resolution in the electron energy loss spectrum (EELS), the vibrational signals were detected at 175.1 meV for h^{11}BN crystals and 179.2 meV for h^{10}BN layers, respectively.[37] These signals are surface phonon polariton, which closely related to the bulk phonon of hBN;[38] thus, their frequency ω naturally depend on the atomic mass μ according to isotope effects ($\omega \propto \sqrt{k/\mu}$, k is the force constant), giving rise to higher ω in h^{10}BN lattices.

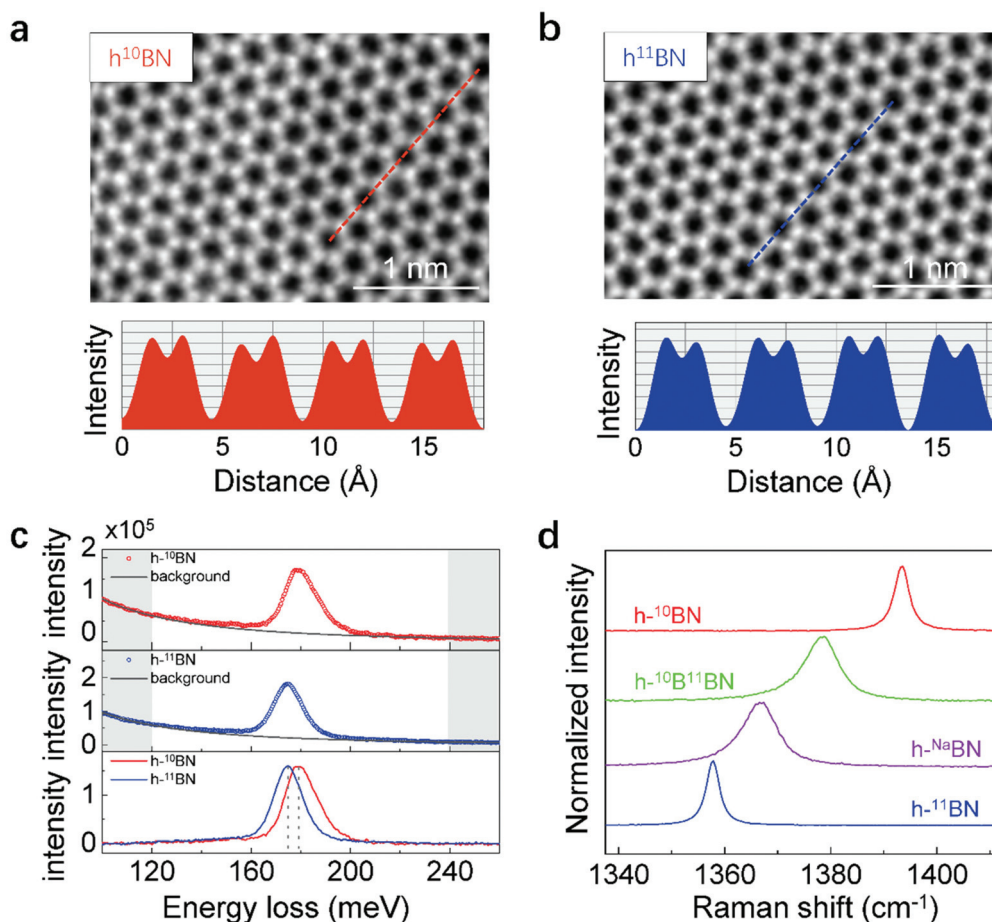The isotopically mixed hBN crystals as required can also be obtained with the Fe flux growth by simply customizing the

Fig. 3 Isotopically engineered hBN crystals. a and b, Atomic high-angle annular dark-field (HAADF) image of multilayer h^{10}BN (a) and h^{11}BN (b), showing no distinguishable difference between them. The image has been denoised using Gaussian blur. c, Vibrational STEM-EELS spectra of h^{10}BN and h^{11}BN, indicating that their vibrational signals are 175.1 and 179.2 meV, respectively. d, Raman spectra of the as-synthesized h^{10}BN, h^{10}B^{11}BN, h^{Na}BN, and h^{11}BN crystals, demonstrating atomic mass-dependent vibrational frequency and mass disorder-induced broadening.

ratio of ^{10}B and ^{11}B powders. As exemplified by the even-mass isotope, i.e., h^{10}B$_{0.5}$^{11}B$_{0.5}$N crystals, a spectrum shift of E$_{2g}$^{high} phonon can be clearly resolved by Raman measurements (Fig. 3d), for example, 1357.8 cm^{-1} for h^{11}BN and 1393.4 cm^{-1} for h^{10}BN. Moreover, isotopically mixed crystals exhibit in-between peak positions: 1366.5 cm^{-1} for h^{Na}BN (natural BN with ~20% of ^{10}B) and 1378.5 cm^{-1} for h^{10}B$_{0.5}$^{11}B$_{0.5}$N.[39,40] Moreover, the isotope purification can depress the Raman line broadening by reducing the static mass disorder, which is apparently displayed in our samples. Specifically, FWHM of h^{10}BN (h^{11}BN) Raman peak is 3.3 cm^{-1} (2.9 cm^{-1}) in comparison with 7.6 cm^{-1} and 7.9 cm^{-1} for h^{10}B$_{0.5}$^{11}B$_{0.5}$N and h^{Na}BN, respectively. More than half cut of Raman linewidths by the isotope purification indicates the minimized phonon-isotope scattering and thus increased phonon lifetime, demonstrating ultrahigh qualities of as-grown crystals.[35,36] Moreover, tuning isotope mixing in BN crystals is of particular interest for quantitatively studying the neutron–^{10}B interaction.

The relevant manifestation at the macroscopic level is the enhancement of thermal conductivity (κ).[41–44] The κ of

1.75 nm-thick h^{11}BN (4L) is measured by the optothermal Raman method.[6–8,45,46] Fig. 4a shows a schematic of the experimental setup for κ measurement. Few-layer h^{11}BN was first transferred above the through hole, which was prefabricated on 90 nm Au-coated Si substrates (Fig. 4b). Then, the 532 nm laser beam was focused in the center of the suspended flake using a 100× objective lens. Increasing the local temperature by partially absorbing laser energy occurs in the vicinity of the laser spot, which can be detected on the basis of Raman frequency shifts, since the in-plane E$_{2g}$^{high} mode is quite sensitive to temperature variation. As shown in Fig. 4c, as the laser power increases, the E$_{2g}$^{high} mode frequency shifts toward lower frequency due to the local laser heating.

The temperature-dependent Raman measurements were performed on the same suspended flake in the temperature control stage for spectroscopy. Fig. 4d shows the E$_{2g}$^{high} mode frequency changes monotonically as a function of temperature (288–418 K with an interval of 10 K). The slope of the corresponding linear fitting is the first-order temperature coefficient of the sample, here −0.02655 ± 0.0009 cm^{-1} K^{-1}. Given that
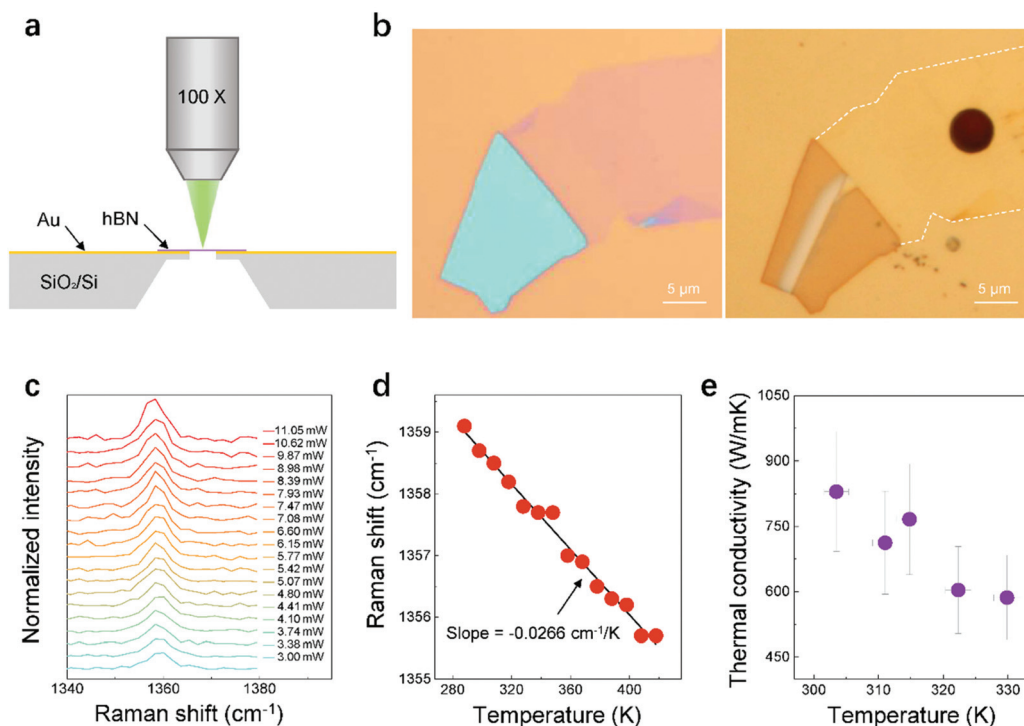
Fig. 4 Thermal conductivity of the suspended few-layer $h^{11}BN$ sheets by the optothermal Raman method. a, Schematic of the experimental setup for the thermal conductivity measurement of the suspended $h^{11}BN$ flake. b, Optical microscopic images of the few-layer $h^{11}BN$ on the SiO_2/Si substrate (left) and Au/Si with prefabricated holes (right). c, Raman spectra under different laser powers. d, Temperature dependence of the in-plane E_{2g}^{high} mode frequency. e, Thermal conductivity of the few-layer $h^{11}BN$ as a function of temperature.

the heat generated by the laser irradiation propagate along the radial direction and the phonon transport is diffusive in the suspended region of the sample, with heat loss from the sample to the surrounding air and *via* radiation ignored, the κ can be calculated as follows:[45]

$$\kappa = \frac{\ln\left(\frac{R}{r_0}\right)}{2\pi d \frac{T_m - T_a}{Q}} \alpha \qquad (1)$$

Here, R is the radius of the through holes (here 2.5 μm), r_0 is the radius of the laser beam spot that is estimated to be 0.31 ± 0.01 μm (ESI Note 1, Fig. S6†), d is the sample thickness, T_m is the temperature measured by Raman, T_a is the ambient temperature, Q is the absorbed laser power, α is the Gaussian profile factor of the laser beam, in our experiment setup, and α is 0.97. The ratio $\frac{T_m - T_a}{Q}$ can be deduced from Fig. 4c, which denotes the temperature rise at the center of the suspended $h^{11}BN$ due to the absorbed laser power. The as-calculated κ are shown in Fig. 4e, where the room-temperature value of the few-layer $h^{11}BN$ is 830 ± 138 W m^{-1} K^{-1}. The error in κ was calculated through the root sum-square error propagation approach.

The high thermal conductivity and isotope enhancement in hBN have been previously reported. Jo *et al.* reported the first experimentally derived κ of 5L and 11L hBN that were ~250 and ~360 W m^{-1} K^{-1} at room temperature, respectively.[47]

Belkerk *et al.* estimated that the κ value of vertically aligned 28 μm-thick BNNTs was as high as 2400 W m^{-1} K^{-1} using an apparent medium theory.[48] Yuan *et al.* measured bulk $h^{10}BN$ crystals and deduced a κ of 585 W m^{-1} K^{-1} at room temperature, ~39% higher than that of bulk $h^{Na}BN$.[43] Recently, Cai *et al.* have used the optothermal Raman method to reveal that the κ value of 1L and 3L $h^{11}BN$ reach up to 1009 and 903 W m^{-1} K^{-1} at room temperature, respectively.[44] Herein, the observed κ value of 830 ± 138 W m^{-1} K^{-1} at room temperature for 1.75 nm-thick $h^{11}BN$ (4L) is comparable to the results reported by Cai *et al.*, and is about 42% and 98% larger than those of bulk $h^{10}BN$ and $h^{Na}BN$, respectively, strongly suggesting the high crystal quality induced by the Fe flux method and successful isotopically engineered growth.

3. Discussion

One conventional wisdom for the low-dimensional materials' growth is learning skills from synthesizing analogous bulk crystals and *vice versa*. Back to the growth of low-dimensional BN, Fe has been shown as a vital catalysis in nitriding; therefore, adding Fe can boost the yield of BN nanotubes.[49,50] On Fe thin films large-area monolayer hBN was grown by CVD.[51] Here, we extend its usage for the metal flux growth of bulk hBN films, and show its reliability, versatility, and high quality of products as well. In comparison with the previously

reported bi-metal flux growth of hBN, the intentional introduction of two metals is to dissolve B and N atoms separately and more. For example, Cr is introduced to dissolving more N, and Ni has high solubility of B atoms, leading to a thicker film and/or, in principle, larger crystal domains.[20] However, in the context of the quaternary phase diagram (for example, Ni–Mo–B–N), the precipitation of hBN could be much more complex, hard to investigate the growth mechanism.[19] Meanwhile, the metal-etching process for thin films' exfoliation can be laborious due to the formation of multi-element alloys. Both challenges can be well addressed by the Fe flux growth.

The convenient achievement of the continuous hBN film in the lab not only provides high-quality crystals in the field of 2D materials research, but also can stimulate the exploration of its large-scale applications. For instance, sandwiched neutron detectors can be fabricated readily with the deposition of both top and bottom metal electrodes.[15,16] Furthermore, in principle, the dimension of products is solely limited by the inner diameter of the furnace tube, making the size extension possible.

4. Conclusion

In summary, we demonstrated the synthesis of high-quality hBN crystals by the Fe flux growth. Single metal as a solvent provides a low-cost and convenient route to high-quality crystals for fundamental research and square-centimeter continuous hBN films towards large-scale applications. The effects of the precursor ratio on grain size and coverage have been symmetrically investigated, giving insights into growth mechanisms. Our method works perfectly as well for the synthesis of isotopically engineered hBN crystals. The achievement of large-scale hBN films in the lab can facilitate hBN-related research in 2D materials and boost the exploration of their large-area applications.

5. Methods

Suspended sample preparation

The through holes in the Si wafer with 300 nm SiO_2 were fabricated by the combination of UV lithography and reactive-ion etching. The diameter of each hole is 5 μm. A thermal evaporator was used to coat the Au film that served as the heat sink. The suspended samples were prepared by a PDMS/PVA (polydimethylsiloxane/polyvinyl alcohol) dry transfer technique. The hBN nanosheets were first exfoliated on silicon substrates with a 300 nm-thick oxide layer. We used the PDMS/PVA membrane to pick up the hBN nanosheet. The PDMS/PVA membrane with the nanosheet was then transferred onto a hole in the Au-coated Si substrate with accurate alignment based on an optical microscope. Subsequently, the PDMS membrane was removed after heating for a few minutes, leaving the PVA/hBN nanosheet in place. Finally, the PVA membrane was removed using deionized water, leaving hBN nanosheets suspended on the hole.

Raman measurements

The SmartRaman confocal-micro-Raman module was used for Raman measurement with a 100× (NA = 0.9) objective lens under the backscattering geometry. The module was developed by the Institute of Semiconductors, Chinese Academy of Sciences, > which is coupled with a Horiba iHR320 spectrometer and a charge-coupled device (CCD) detector. The excitation wavelength was 532 nm. All Raman spectra were calibrated with the Raman peak of Si at 520.7 cm^{-1}. The laser power passing the objective lens was measured using a semiconductor laser power meter (Newport, model 1916-C). For the temperature-dependent RamanPB4 heating stage was employed. In all temperature-dependent and laser power-dependent Raman measurements, a 100× objective lens with a numerical aperture of 0.8 was used.

TEM experiments

TEM experiments were carried out using a monochromatic Nion U-HERMES200 electron microscope operating at 60 kV. STEM-EELS experiments were performed in an aloof configuration (details shown in ESI Fig. 7†) with convergence semi-angle α = 15 mrad and collection semi-angle β = 24.9 mrad. The energy resolution was ∼8 meV, and the beam current was ∼12 pA.[38,52] HAADF images were both acquired under the conditions of α = 35 mrad and β = (80, 210) mrad operating at 60 kV.

Author contributions

L. L. and Y. L. conceived the project. Y. L., X. W., C. T., R. L., H. T., and Z. Y. prepared samples. Y. L. and R. L. completed the sample transfer. P. L., S. Y., S. L., Z. L., and Y. H. fabricated substrates for thermal conductivity measurements. Y. L. and X. H. performed the Raman measurements. N. L., J. G., P. G., and L. W. performed the HAADF and STEM-EELS characterizations. Y. L., X. W., C. T., S. B., and L. L. analyzed data. Y. L. and L. L. wrote the manuscript, and all authors discussed and commented on it.

Conflicts of interest

There are no conflicts to declare.

Acknowledgements

Notes and references

1 J. D. Caldwell, I. Aharonovich, G. Cassabois, J. H. Edgar, B. Gil and D. N. Basov, *Nat. Rev. Mater.*, 2019, **4**, 552–567.

2 C. R. Dean, A. F. Young, I. Meric, C. Lee, L. Wang, S. Sorgenfrei, K. Watanabe, T. Taniguchi, P. Kim, K. L. Shepard and J. Hone, *Nat. Nanotechnol.*, 2010, **5**, 722–726.

3 L. Wang, I. Meric, P. Y. Huang, Q. Gao, Y. Gao, H. Tran, T. Taniguchi, K. Watanabe, L. M. Campos, D. A. Muller, J. Guo, P. Kim, J. Hone, K. L. Shepard and C. R. Dean, *Science*, 2013, **342**, 614–617.

4 X. X. Xi, Z. F. Wang, W. W. Zhao, J. H. Park, K. T. Law, H. Berger, L. Forro, J. Shan and K. F. Mak, *Nat. Phys.*, 2016, **12**, 139–143.

5 L. Britnell, R. V. Gorbachev, R. Jalil, B. D. Belle, F. Schedin, A. Mishchenko, T. Georgiou, M. I. Katsnelson, L. Eaves, S. V. Morozov, N. M. R. Peres, J. Leist, A. K. Geim, K. S. Novoselov and L. A. Ponomarenko, *Science*, 2012, **335**, 947–950.

6 Z. Y. Lin, C. R. Liu and Y. Chai, *2D Mater.*, 2016, **3**, 041009.

7 Q. R. Cai, D. Scullion, W. Gan, A. Falin, S. Y. Zhang, K. Watanabe, T. Taniguchi, Y. Chen, E. J. G. Santos and L. H. Li, *Sci. Adv.*, 2019, **5**, 0129.

8 I. Jo, M. T. Pettes, J. Kim, K. Watanabe, T. Taniguchi, Z. Yao and L. Shi, *Nano Lett.*, 2013, **13**, 550–554.

9 H. Q. Zhou, J. X. Zhu, Z. Liu, Z. Yan, X. J. Fan, J. Lin, G. Wang, Q. Y. Yan, T. Yu, P. M. Ajayan and J. M. Tour, *Nano Res.*, 2014, **7**, 1232–1240.

10 M. T. Alam, M. S. Bresnehan, J. A. Robinson and M. A. Haque, *Appl. Phys. Lett.*, 2014, **104**, 013113.

11 C. R. Wang, J. Guo, L. Dong, A. Aiyiti, X. F. Xu and B. W. Li, *Sci. Rep.*, 2016, **6**, 25334.

12 C. Y. Zhi, Y. Bando, C. C. Tang, H. Kuwahara and D. Golberg, *Adv. Mater.*, 2009, **21**, 2889–2893.

13 H. M. Fang, S. L. Bai and C. P. Wong, *Composites, Part A*, 2017, **100**, 71–80.

14 K. Watanabe, T. Taniguchi, T. Niiyama, K. Miya and M. Taniguchi, *Nat. Photonics*, 2009, **3**, 591–594.

15 T. C. Doan, S. Majety, S. Grenadier, J. Li, J. Y. Lin and H. X. Jiang, *Nucl. Instrum. Methods Phys. Res., Sect. B*, 2014, **748**, 84–90.

16 A. Maity, S. J. Grenadier, J. Li, J. Y. Lin and H. X. Jiang, *Appl. Phys. Lett.*, 2020, **116**, 142102.

17 J. S. Lee, S. H. Choi, S. J. Yun, Y. I. Kim, S. Boandoh, J. H. Park, B. G. Shin, H. Ko, S. H. Lee, Y. M. Kim, Y. H. Lee, K. K. Kim and S. M. Kim, *Science*, 2018, **362**, 817–821.

18 L. Wang, X. Xu, L. Zhang, R. Qiao, M. Wu, Z. Wang, S. Zhang, J. Liang, Z. Zhang, Z. Zhang, W. Chen, X. Xie, J. Zong, Y. Shan, Y. Guo, M. Willinger, H. Wu, Q. Li, W. Wang, P. Gao, S. Wu, Y. Zhang, Y. Jiang, D. Yu, E. Wang, X. Bai, Z. J. Wang, F. Ding and K. Liu, *Nature*, 2019, **570**, 91–95.

19 Y. Kubota, K. Watanabe, O. Tsuda and T. Taniguchi, *Science*, 2007, **317**, 932–934.

20 T. B. Hoffman, B. Clubine, Y. Zhang, K. Snow and J. H. Edgar, *J. Cryst. Growth*, 2014, **393**, 114–118.

21 S. Liu, R. He, Z. P. Ye, X. Z. Du, J. Y. Lin, H. X. Jiang, B. Liu and J. H. Edgar, *Cryst. Growth Des.*, 2017, **17**, 4932–4935.

22 S. Liu, R. He, L. J. Xue, J. H. Li, B. Liu and J. H. Edgar, *Chem. Mater.*, 2018, **30**, 6222–6225.

23 J. H. Li, C. Yuan, C. Elias, J. Y. Wang, X. T. Zhang, G. H. Ye, C. R. Huang, M. Kuball, G. Eda, J. M. Redwing, R. He, G. Cassabois, B. Gil, P. Valvin, T. Pelini, B. Liu and J. H. Edgar, *Chem. Mater.*, 2020, **32**, 5066–5072.

24 N. Zhang, N. Yang, W. Wang, X. Zhong and X. Chen, *J. Cryst. Growth*, 2021, **562**, 126074.

25 M. Yano, Y. K. Yap, M. Okamoto, M. Onda, M. Yoshimura, Y. Mori and T. Sasaki, *Jpn. J. Appl. Phys.*, 2000, **39**, L300–L302.

26 J. H. Li, J. Y. Wang, X. T. Zhang, C. Elias, G. H. Ye, D. Evans, G. Eda, J. M. Redwing, G. Cassabois, B. Gil, P. Valvin, R. He, L. Bin and J. H. Edgar, *ACS Nano*, 2021, **15**, 7032–7039.

27 L. Liu, J. Park, D. A. Siegel, K. F. McCarty, K. W. Clark, W. Deng, L. Basile, J. C. Idrobo, A. P. Li and G. Gu, *Science*, 2014, **343**, 163–167.

28 A. Mohsin, N. G. Cross, L. Liu, P. Z. Liu, G. Duscher and G. Gu, *Phys. Status Solidi B*, 2017, **254**, 1700069.

29 L. Liu, D. A. Siegel, W. Chen, P. Z. Liu, J. J. Guo, G. Duscher, C. Zhaog, H. Wang, W. L. Wang, X. D. Bai, K. F. McCarty, Z. Y. Zhang and G. Gu, *Proc. Natl. Acad. Sci. U. S. A.*, 2014, **111**, 16670–16675.

30 P. Z. Liu, H. F. Tian, W. Windl, G. Gu, G. Duscher, Y. C. Wu, M. Zhao, J. J. Guo, B. S. Xu and L. Liu, *Nanoscale*, 2019, **11**, 20676–20684.

31 Y. Huang, Y. H. Pan, R. Yang, L. H. Bao, L. Meng, H. L. Luo, Y. Q. Cai, G. D. Liu, W. J. Zhao, Z. Zhou, L. M. Wu, Z. L. Zhu, M. Huang, L. W. Liu, L. Liu, P. Cheng, K. H. Wu, S. B. Tian, C. Z. Gu, Y. G. Shi, Y. F. Guo, Z. G. Cheng, J. P. Hu, L. Zhao, G. H. Yang, E. Sutter, P. Sutter, Y. L. Wang, W. Ji, X. J. Zhou and H. J. Gao, *Nat. Commun.*, 2020, **11**, 2453.

32 M. Cardona, *Top. Appl. Phys.*, 1982, 254.

33 O. Kubaschewski, *IRON—Binary Phase Diagrams*, Springer-Verlag, 1982.

34 M. Cardona and M. L. W. Thewalt, *Rev. Mod. Phys.*, 2005, **77**, 1173–1224.

35 T. Q. P. Vuong, S. Liu, A. Van der Lee, R. Cusco, L. Artus, T. Michel, P. Valvin, J. H. Edgar, G. Cassabois and B. Gil, *Nat. Mater.*, 2018, **17**, 152–158.

36 A. J. Giles, S. Y. Dai, I. Vurgaftman, T. H. Man, S. Liu, L. Lindsay, C. T. Ellis, N. Assefa, I. Chatzakis, T. L. Reinecke, J. G. Tischler, M. M. Fogler, J. H. Edgar, D. N. Basov and J. D. Caldwell, *Nat. Mater.*, 2018, **17**, 134–139.

37 R. S. Qi, N. Li, J. L. Du, R. C. Shi, Y. Huang, X. X. Yang, L. Liu, Z. Xu, Q. Dai, D. P. Yu and P. Gao, *Nat. Commun.*, 2021, **12**, 1179.

38 N. Li, X. D. Guo, X. X. Yang, R. S. Qi, T. Y. Qiao, Y. F. Li, R. C. Shi, Y. H. Li, K. H. Liu, Z. Xu, L. Liu, F. J. G. de Abajo, Q. Dai, E. G. Wang and P. Gao, *Nat. Mater.*, 2021, **20**, 43–48.

39 R. Cusco, L. Artus, J. H. Edgar, S. Liu, G. Cassabois and B. Gil, *Phys. Rev. B*, 2018, **97**, 155435.

40 R. Cusco, J. H. Edgar, S. Liu, G. Cassabois, B. Gil and L. Artus, *Phys. Rev. B*, 2019, **99**, 085428.

41 S. Barman, *EPL*, 2011, **96**, 16004.

42 L. Lindsay and D. A. Broido, *Phys. Rev. B: Condens. Matter Mater. Phys.*, 2011, **84**, 155421.

43 C. Yuan, J. H. Li, L. Lindsay, D. Cherns, J. W. Pomeroy, S. Liu, J. H. Edgar and M. Kuball, *Commun. Phys.*, 2019, **2**, 43.

44 Q. R. Cai, D. Scullion, W. Gan, A. Falin, P. Cizek, S. Liu, J. H. Edgar, R. Liu, L. H. Li, B. C. C. Cowie and E. J. G. Santos, *Phys. Rev. Lett.*, 2020, **125**, 085902.

45 W. W. Cai, A. L. Moore, Y. W. Zhu, X. S. Li, S. S. Chen, L. Shi and R. S. Ruoff, *Nano Lett.*, 2010, **10**, 1645–1651.

46 J. U. Lee, D. Yoon, H. Kim, S. W. Lee and H. Cheong, *Phys. Rev. B: Condens. Matter Mater. Phys.*, 2011, **83**, 081419.

47 I. Jo, M. T. Pettes, J. Kim, K. Watanabe, T. Taniguchi, Z. Yao and L. Shi, *Nano Lett.*, 2013, **13**, 550–554.

48 B. E. Belkerk, A. Achour, D. Y. Zhang, S. Sahli, M. A. Djouadi and Y. K. Yap, *Appl. Phys. Express*, 2016, **9**, 075002.

49 L. Li, L. H. Li, Y. Chen, X. J. J. Dai, T. Xing, M. Petravic and X. W. Liu, *Nanoscale Res. Lett.*, 2012, **7**, 417.

50 C. C. Tang, M. L. de la Chapelle, P. Li, Y. M. Liu, H. Y. Dang and S. S. Fan, *Chem. Phys. Lett.*, 2001, **342**, 492–496.

51 S. Caneva, R. S. Weatherup, B. C. Bayer, B. Brennan, S. J. Spencer, K. Mingard, A. Cabrero-Vilatela, C. Baehtz, A. J. Pollard and S. Hofmann, *Nano Lett.*, 2015, **15**, 1867–1875.

52 Y. H. Li, R. S. Qi, R. C. Shi, N. Li and P. Gao, *Sci. Bull.*, 2020, **65**, 820–826.